Physica Scripta

PAPER

Investigation of raman spectrum, structural, morphological, and optical features of Fe_2O_3 and Fe_2O_3/reduced graphene oxide hybrid nanocomposites

RECEIVED
3 July 2022

REVISED
19 August 2022

ACCEPTED FOR PUBLICATION
20 October 2022

PUBLISHED
1 November 2022

Ahmed I Abdel-Salam[1], **Islam Gomaa**[1], **A Khalid**[2] **and T S Soliman**[3,4,*]

[1] Nanotechnology Research Center (NTRC), The British University in Egypt (BUE), El Shorouk City, Suez Desert Road, P.O. Box 43, Cairo 11837, Egypt
[2] Department of Basic Engineering Sciences, Faculty of Engineering (Shoubra), Benha University, Benha, Egypt
[3] Physics Department, Faculty of Science, Benha University, Benha 13518, Egypt
[4] Institute of Natural Sciences and Mathematics, Ural Federal University, Ekaterinburg 620000, Russia
[*] Author to whom any correspondence should be addressed.

E-mail: tarek.attia@fsc.bu.edu.eg

Keywords: Fe_2O_3-rGO nanocomposites, refractive index, raman spectroscopy, TEM

Abstract

The Hematite (Fe_2O_3) nanoparticles and Fe_2O_3-reduced graphene oxide (rGO) nanocomposite were successfully synthesized via co-precipitation method. The rGO was used as passivation layer to improve the optical properties of the Fe_2O_3. X-ray diffraction, transmission electron microscopy, Raman, and Fourier transform-infrared spectroscopy were used to investigate the modification in the Fe_2O_3 structure in the presence of rGO. UV-visible absorption spectra were investigated, and the optical bandgap was determined. Using different relations like Moss, Rivandra, Anani, and others, the refractive index was calculated depending on the obtained optical bandgap. The refractive index values were compared with the data calculated from Duffy relation and good accordance was found between them. The optical bandgap and electronegativity were found to decrease by the addition of rGO in Fe_2O_3 matrix, while the refractive index was found to increase. Consequently, the Fe_2O_3-rGO nanocomposites capacity to control optical properties makes it a perfect contender for a variety of applications.

1. Introduction

Because of their unique features and wide range of uses, the synthesis of nanostructures with distinct properties has attracted a lot of interest recently [1–4]. The shape of materials has a considerable impact on the physical, chemical, and optical characteristics of nanoparticles [5–7]. Owing to the effect of the morphological shape of the synthesized nanoparticles (NPs), Scientists are interested in manufacturing NPs in different shapes rather than the spherical one for the various uses in morphology-dependent applications like sensing and biomedical [8,9].

Transition metal oxides such as TiO_2, MnO_2, and Fe_2O_3 have been explored previously as supercapacitor electrode materials [10–12]. Fe_2O_3 is considered as suitable candidate materials in many applications such as; absorbing material in the solar cell, sensors, data-storage, photo-catalyst, magnetic recording, bio-imaging, and others [11, 13–17]. Fe_2O_3 has an energy gap ~ 2.1 eV [4], low cost, non-toxic, easy to prepare, good stability, and environmentally safe [15,18]. Otherwise, Fe_2O_3 NPs have unique characteristics including electrical, thermal, mechanical, and high surface area [13,15, 18]. Hence, Fe_2O_3 is one of the preferred semiconductors in electronic applications.

There is no doubt that graphene has captivated the scientific community's interest. Graphene oxide (GO) is a semiconductor with bandgap ~ 2.2 eV which transform to reduced graphene oxide (rGO) with lower bandgap ranging from 1 to 1.69 eV [19, 20]. This process of the reduction of GO is to increase the absorption efficiency, which give the material importance to be used in various optoelectronic application. As a natural outcome,

graphene is often chosen in a variety of multiple disciplines including electronics, magnetics, and optics [21, 22]. Previously CdSe-rGO nanocomposite was fabricated with different particle size of CdSe and was found to tune the optical parameters via the controlling their particle sizes [23]. Guo *et al* [24] reported the distribution of SO_2 nanoparticles on the graphene matrix and was found that GO with high reduction degree improves the conductivity and enhance the matrix properties. Nosheen *et al* [25] reported CdS ancored on graphene surface to form CdS-rGo using DMF to improve the effective electrode materials for application in solid state dye sensitized solar cells.

Herein Fe_2O_3 NPs were successfully synthesized and decorated onto graphene surface to expand the application range and improve their characteristics. The Fe_2O_3 NPs are rapidly moved to graphene sheets, enhancing its charge transfer rate and optical properties [26].

The main objective of the present study is to examine the influence of graphene sheets on the structure and optical characteristics of Fe_2O_3 NPs. The optical parameters like refractive index and optical bandgap are important factors of communication and information technological innovation [27]. The structural, morphological, and optical properties of Fe_2O_3 NPs and Fe_2O_3-rGO nanocomposite are studied using FTIR, Raman, XRD, TEM, and UV-visible spectroscopy.

2. Experimental work

2.1. Chemicals and reagents

All chemicals, Iron (III) chloride anhydrous (Fisher chemical, 98%), ammonia solution (Fisher chemical, 35%), Poly vinyl alcohol (Sigma Aldrich, 86%–89% hydrolyzed, high molecular weight (80,000–120,000)), and deionized (DI) Milli-Q water were used without further purification.

2.2. Synthesis of Fe_2O_3 NPs

Fe_2O_3 NPs were prepared via the coprecipitation method [28]. A solution of 1 M $FeCl_3$in DI water (100 ml) was heated to 80 °C. Then, 25% ammonia solution was added drop by drop with continuous stirring for 2 h. Finally, the prepared solution was centrifuged at 8000 rpm and the precipitated particles collected and then washed by the DI water. The collected particles were dried in the oven at 80 °C for 24 h followed by calcination at 400 °C for 4 h.

2.3. Synthesis of Fe_2O_3-rGO Nanocomposites

The graphene oxide (GO) was prepared previously using improved Hummers' method, as described elsewhere, followed by lyophilization process to increase the surface area of the GO sheets [29]. Fe_2O_3-rGO nanocomposites were prepared by mixing 0.6 gm of the as-prepared Fe_2O_3 with 0.3 gm GO in 100 ml DI water. Then, the mixture was sonicated via ultra-prop sonication (Sonochemical method) for 15 min at 600 Watt. Finally, the obtained Fe_2O_3-rGO nanocomposite was dispersed in distilled water (5 ml) and dried in a vacuum oven at 80 °C for 12 h before being collected as a powder.

2.4. Characterizations

Panalytical Empyrean x-ray diffractometer (XRD), Malvern Panalytical Ltd-Netharlands, was equipped with Cu-Kα1 radiation; $\lambda = 0.154056$ nm. The XRD patterns were collected in 2θ range from 0° to 80° (scan step/scanning time = 0.02°/0.5s at room temperature). The TEM images of the samples were performed using transmission electron microscope (Joel JEM-2100, Japan) operated at 200 kV. UV-Visible absorption spectra of the samples were operated using a double beam spectrophotometer (Perkin Elmer Lambda 40, USA). The measurements were done in the range from 200 nm to 800 nm with an accuracy ±0.8 nm. Fourier transform infrared spectrometer (FTIR), Vertex 70-Bruker-Germany, was used to investigate the change in the bonds structure in a spectral range of 4000–400 cm^{-1} with a spectral resolution of 4 cm^{-1}. Raman spectra of GO, Fe_2O_3, Fe_2O_3-rGO were investigated via Raman spectroscopy model WiTec-Alpha-300-AR- Germany, with spectral resolution 0.72 cm^{-1}.

3. Results and discussion

3.1. XRD Analysis

Figure 1 show XRD patterns of pure GO, synthesized Fe_2O_3 NPs, and Fe_2O_3-rGO nanocomposite. The pattern profiles indicated the seven characteristic diffraction peaks of the Rhombohedral Fe_2O_3 phase with space group: R-3c (JCPDS No. 01–076–8394). These observed peaks at 24.13°, 33.15°, 35.62°, 40.86°, 49.45°, 54.06° and 57.59° are assigned to (012), (104), (110), (113), (024), (116), and (018) planes, respectively. The same peaks are observed for Fe_2O_3-rGO nanocomposite with a little shift to higher angles.

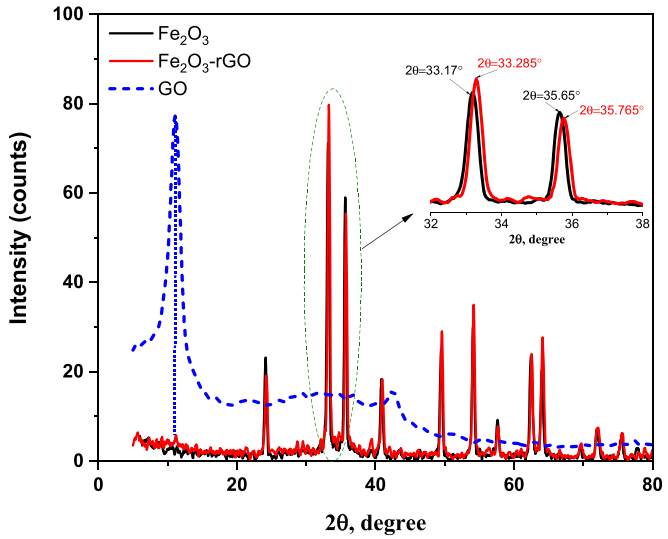

Figure 1. XRD spectra of GO, Fe_2O_3, and Fe_2O_3-rGO nanocomposite.

Introducing rGO to the Fe_2O_3 nanocomposite shows a shift to higher angles in the XRD pattern. The inset of figure 1 shows the two main characteristic peaks at 33.17° and 35.65° shifted to 33.285° and 35.765° respectively. This slight shift in the angle of diffraction is an indication to the change in the lattice structure and complexation between the Fe_2O_3 NP and the rGO. The crystallite size was calculated using the Scherrer equation [18] and was found to be ~ 22 nm for Fe_2O_3 and 21 nm for Fe_2O_3-rGO nanocomposite.

Williamson-Hall method was used to investigate the crystallite size (D), the micro-strain (ε), and the dislocation density (δ). The relation of Williamson-Hall represented as follow [30, 31],

$$\beta \cos(\theta) = \frac{k\,\lambda}{D} + 4\varepsilon \sin(\theta) \tag{1}$$

$$\delta = \frac{1}{D^2} \tag{2}$$

where β is the full-width at half maximum and k is shape factor ~ 0.9. The relation between $\beta\cos(\theta)$ on Y-axis and 4 $\sin(\theta)$ on X-axis is represented in figure 2. It shows a linear relation with a slope equal to the micro-strain and the intercept equal to $k\lambda/D$. The D, ε, and δ values are investigated and represented in table 1.

As shown in table 1, the particle size decreases which confirmed by the shift in peaks angle in XRD pattern. The d-spacing decreases because of the shift in diffraction angles to higher values. Also, the negative value of strain confirms the compression of the material. Consequently, the length decreases, shrinking in the particle size, and the cross-section area increases. In addition, the data calculated using Scherrer equation is in a good agreement with Williamson-Hall plot. The XRD pattern of the pure GO, figure 2, exhibited a strong peak at $2\theta = 11.13°$, which indexed to (001) plane with d-spacing ~8.03 Å (via Bragg's equation) [32]. While this peak disappears in the Fe_2O_3-rGO nanocomposites. This can be related to the transformation of the most of GO to the reduced graphene oxide rGO and the groups bonded with oxygen (C–OH, COOH, C=O) are removed [32]. The decrease of the crystallite size may be caused by the rGO sheets which hindered the growth of Fe_2O_3 NPs and reduced its agglomeration which in good agreement with the literature [33].

3.2. TEM Analysis

TEM analysis was used to investigate the Fe_2O_3 and Fe_2O_3-rGO structure, particle sizes, and distinguish their morphology. Figure 3 shows the TEM images for Fe_2O_3 and Fe_2O_3-rGO nanocomposites.

Figure 3(a) shows Fe_2O_3 NP in a semi-spherical shape with an average particle size approximately ~32.44 nm. The alliance of high surface energy with tiny ones is mainly responsible for nanoparticles agglomeration. Also, it may be due to the absence of capping agent which is responsible for controlling the shape and size of the nanomaterials. Figure 3(d) displays the TEM image of Fe_2O_3–rGO hybrid composite; the hybrid nanocomposites consist of two-dimensional rGO sheets decorated with Fe_2O_3 NPs. It shows that a significant number of Fe_2O_3 NPs are irregular in shape with an average size of 28.65 nm decorated on rGO sheet which serves as a platform. The TEM image of the GO sheet is shown in our previous article [23]. Obviously, the Fe_2O_3 NPs growth are hindered by the rGO sheet, and the particle size decreases as well. This is in good agreement with the literature [34]. Moreover, the distribution of Fe_2O_3 NPs on the rGO surface may increase the stability of the

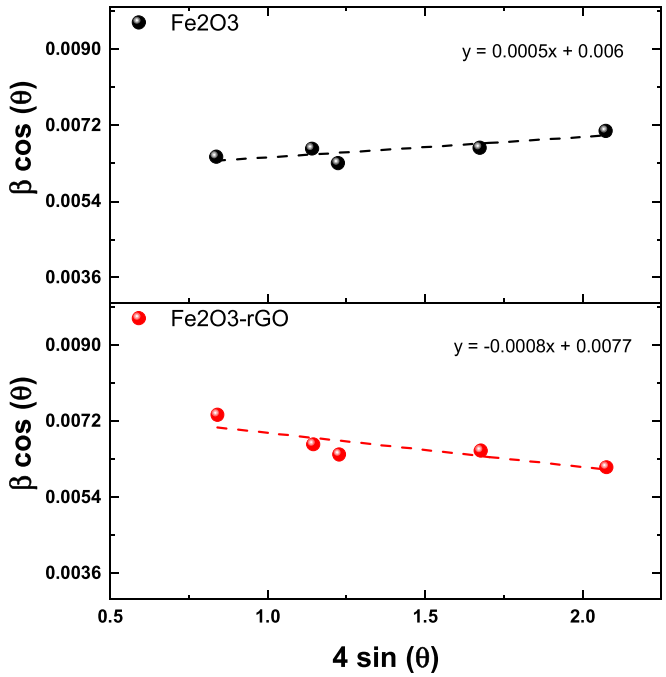

Figure 2. Williamson-Hall plots of Fe_2O_3, and Fe_2O_3-rGO nanocomposite.

Table 1. Crystallite size (D), strain (ε), and dislocation density (δ).

Sample	D (nm)	ε	$\delta, \times 10^{15}$ (m^{-2})
Fe_2O_3	23	0.0005	1.87
Fe_2O_3-rGO	18	−0.0008	3.08

Fe_2O_3-rGO nanocomposites. The high-resolution TEM (HRTEM) images of the Fe_2O_3 and Fe_2O_3-rGO, figures 3(b) and (e), show lattice fringes of about 0.25 nm. This is consistent with the inter-planar spacing of (110) planes of the Rhombohedral Fe_2O_3 (JCPDS No. 01–076–8394). This result is coincided with the XRD data. Furthermore, the inter-planar spacing derived from the polycrystalline Selected Area Electron Diffraction (SAED) pattern for the Fe_2O_3 and Fe_2O_3-rGO are consistent with the Rhombohedral Fe_2O_3 (JCPDS No. 01–076–8394), see figures 3(c) and (f). Furthermore, from the particle size distribution, figures 3(g)–(h), the average particle sizes are 32 nm for Fe_2O_3 and 28 nm for Fe_2O_3-rGO. This result is slightly accordance with the crystallite sizes calculated from XRD.

3.3. FTIR analysis

Figure 4 shows the FTIR spectra of the GO, Fe_2O_3 NPs, and Fe_2O_3-rGO nanocomposite. The FT-IR spectra of the Fe_2O_3-rGO nanocomposite revealed distinct peaks at about 520, 436 cm^{-1} are assigned to the stretching vibration of Fe-O bond of the Fe_2O_3 nanoparticles. Furthermore, the peaks appeared at 1731, 1614 cm^{-1} are characteristic for the C=O and C=C group of the rGO, respectively. It confirms the loading of the Fe_2O_3 on the GO sheets, as well as the very low intensity of the C=O peak in the FT-IR spectra of the Fe_2O_3-rGO confirming reduction of the GO into rGO during the ultra-sonication process [23, 35].

3.4. Raman analysis

The as prepared Fe_2O_3, Fe_2O_3-rGO, and GO was investigated using Raman spectroscopy, as shown in figure 5. The Fe_2O_3-rGO nanocomposite shows two definite peaks at 1342 cm^{-1} and 1586 cm^{-1}, which correspond to the D and G bands of the rGO, respectively, with intensity ratio (I_D/I_G) equal 1.4; this ratio is slightly higher than that of GO, which is 0.94 [16, 17]. The increase in the intensity ratio (I_D/I_G) for the Fe_2O_3-rGO might be due to elimination of the oxygen-containing functional groups from the GO sheets, indicating that the GO was reduced during formation of the Fe_2O_3-rGO as a result of the ultra-sonication process [16, 17]. The Fe_2O_3-rGO reveals distinctive peak at 493 cm^{-1} corresponding to the A_{1g} vibration mode, and peaks at 404 cm^{-1} and 604 cm^{-1} corresponding to the E_g vibration mode, but the peaks have lower intensities compared to the Fe_2O_3.

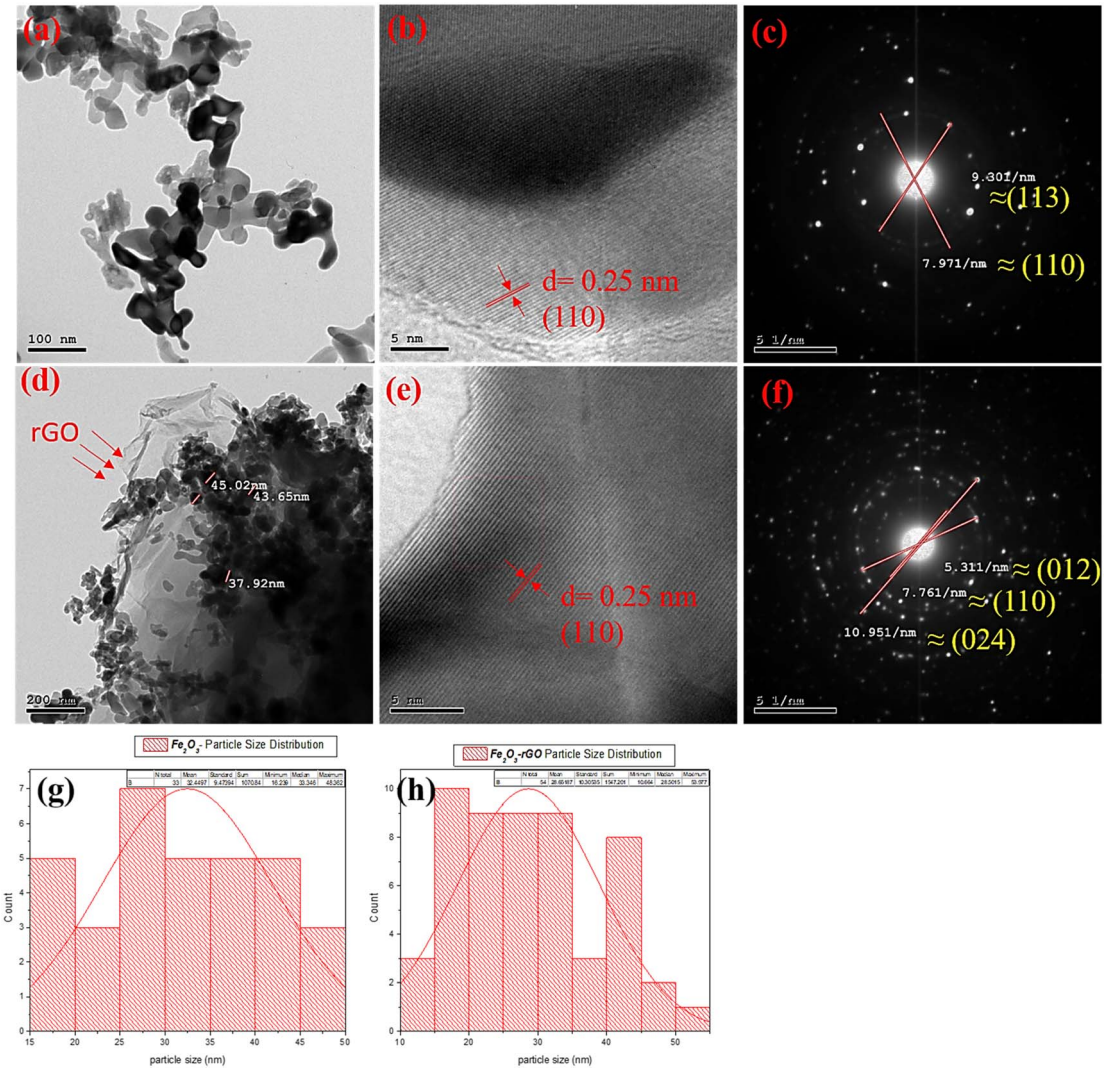

Figure 3. (a), (d) TEM images, (b), (e) HRTEM images, (c), (f) SEAD pattern, and (g), (h) the histogram of Fe_2O_3 & Fe_2O_3-rGO, respectively.

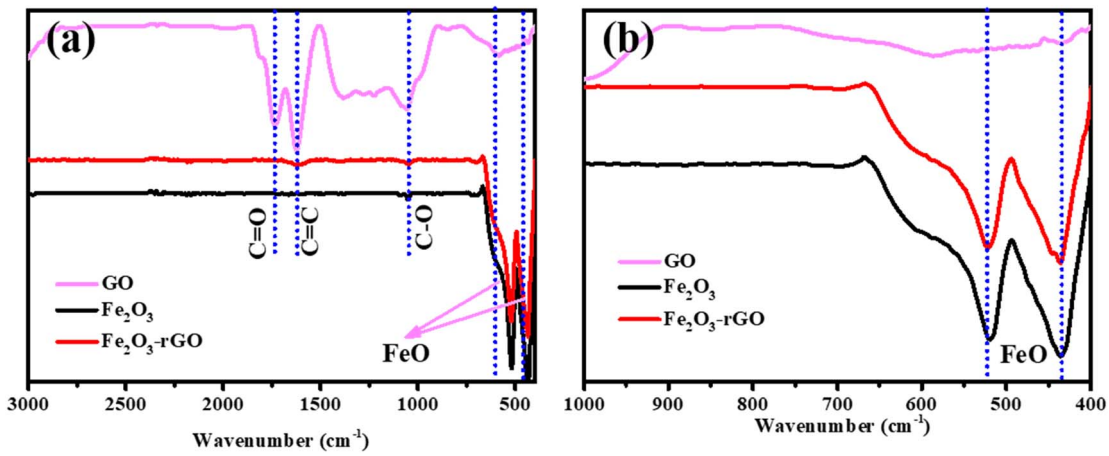

Figure 4. FTIR spectra of GO, Fe_2O_3, and Fe_2O_3-rGO nanocomposite at different spectral ranges.

3.5. Optical properties

Figure 6 shows the UV–visible absorption spectra of the Fe_2O_3, Fe_2O_3-rGO nanocomposite, and GO.

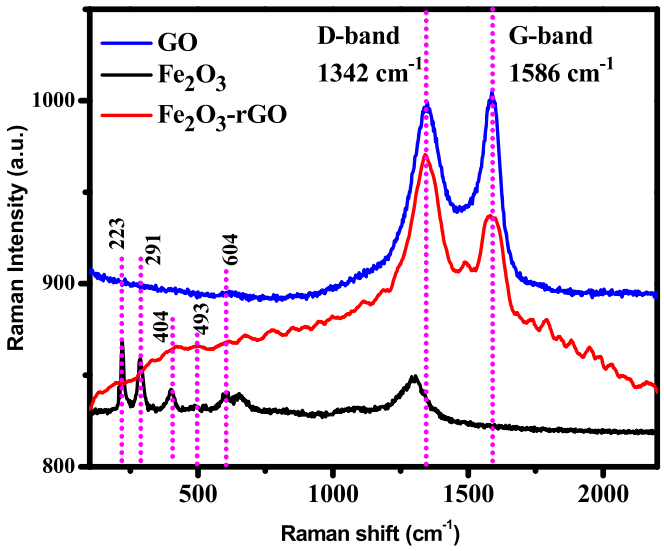

Figure 5. Raman spectra of Fe_2O_3 and Fe_2O_3-rGO nanocomposite.

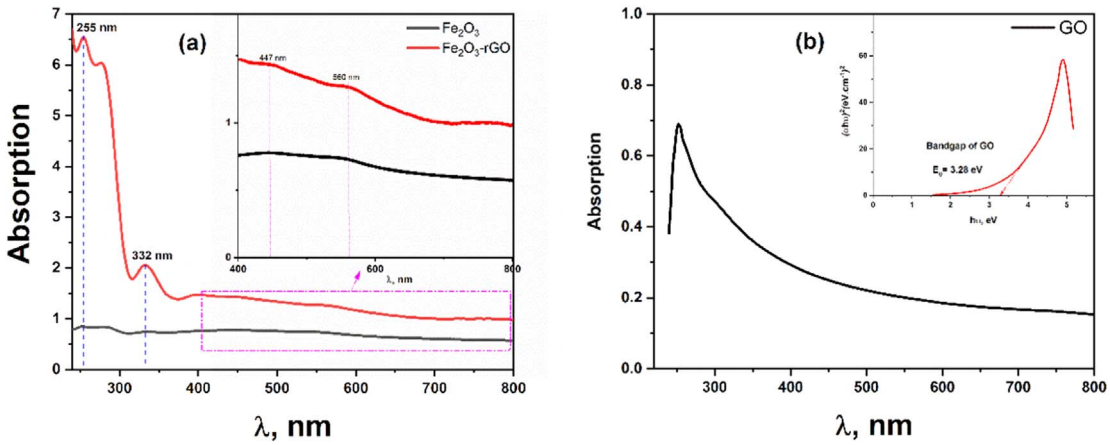

Figure 6. The absorption spectra for; (a) Fe_2O_3, Fe_2O_3-rGO nanocomposite and (b) GO.

Figure 6 shows the UV–visible absorption spectra of graphene oxide, Fe_2O_3 NPs, and Fe_2O_3-rGO nanocomposite. In figure 6(a) two absorption bands are observed clearly for Fe_2O_3-rGO at 255 nm and 332 nm related to π–π^* (C=C bonds) and n-π^* (C=O bonds) transitions, respectively [36]. In the UV region, an absorption edge is observed for Fe_2O_3 NPs. This absorption edge is more pronounced and sharper with the insertion of rGO to the matrix. The absorption edge in the range from 340 to 360 nm is related to the transition within the rGO sheets. Figure 6(b) shows the absorption spectrum of GO with an absorption edge extended from 250 nm to 600 nm. Extrapolating the absorption edge intercept with the *X*-axis at ~ 378 nm ($E_g = 1240/378 = 3.28$ eV). The inset of figure 6(b) shows the direct optical bandgap which is approximately ~ 3.28 eV. This result is in good agreement with the literature [37]. While the wide halo in the visible region is attributed to the surface plasmon resonance which caused by Fe^{+3} ions in Fe_2O_3 NPs [38]. Moreover, two bands are observed at 447 nm and 560 nm in the visible region (inset figure 6(a)). These bands become more pronounced with the insertion of rGO to the matrix [19]. These confirms the effect of the rGO sheets on the Fe_2O_3 NPs to absorb more energy [35] in the UV-visible region which is very useful in various optical applications especially for the solar cells. Also, in the visible region, absorption edge is observed in the range from 570 nm to 700 nm. This absorption edge shifted towards the higher wavelength region for Fe_2O_3-rGO nanocomposite. This indicates the decrease of the material bandgap.

The optical parameters like; the absorption coefficient (α) and optical bandgap (E_g) are important for electronic application, which can be investigated by Tauc's relation as follow,

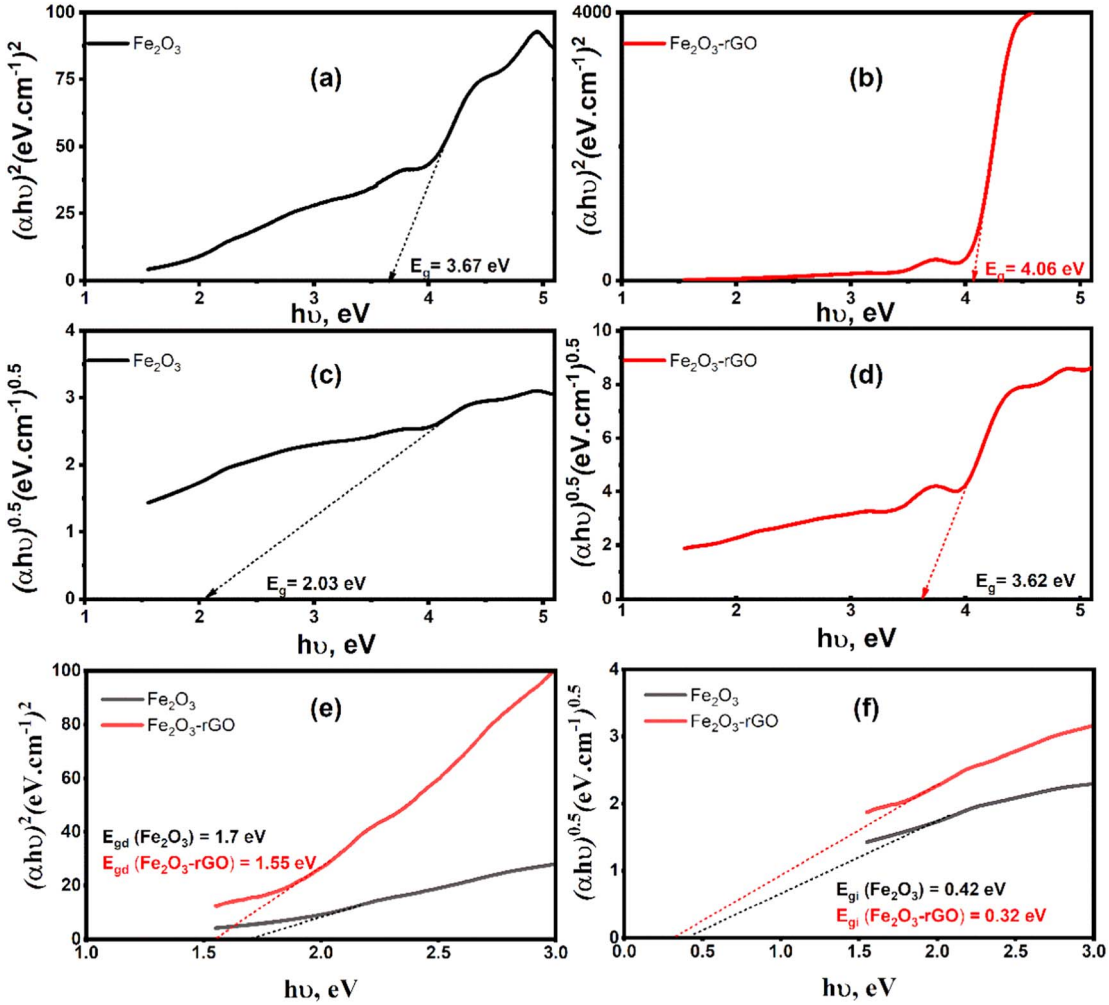

Figure 7. Plots of $(\alpha h\upsilon)^2$ & $(\alpha h\upsilon)^{0.5}$ versus $(h\upsilon)$ for the synthesized Fe_2O_3 and Fe_2O_3-rGO NPs.

Table 2. Optical bandgaps in the UV and visible regions; (E_{gd1} & E_{gd2} for direct) and (E_{gi1} & E_{gi2} for indirect)

	UV-region		Visible region	
Composition	E_{gd1}, eV	E_{gi1}, eV	E_{gd2}, eV	E_{gi2}, eV
Fe_2O_3	3.67	2.03	1.70	0.42
Fe_2O_3-rGO	4.08	3.62	1.55	0.32

$$\alpha h\upsilon = B(h\upsilon - E_g)^m \tag{3}$$

where $h\upsilon$ is the incident photons energy, B is a constant, and m is index number depend on the type of electronic transition ($m = 1/2, 2$ for direct and indirect transitions, respectively). The relation between $(\alpha h\upsilon)^2$ & $(\alpha h\upsilon)^{0.5}$ versus $(h\upsilon)$ are shown in figure 7. The optical bandgap values were extracted from the plots and tabulated in table 2.

In the UV-region the bandgap was found to increase from 3.67 eV for Fe_2O_3 to 4.06 eV for Fe_2O_3-rGO (direct) and from 2.03 for Fe_2O_3 to 3.62 eV for Fe_2O_3-rGO (indirect). While, in the visible region, the bandgap was found to decrease from 1.7 eV for Fe_2O_3 to 1.5 eV for Fe_2O_3-rGO (direct) and from 0.42 eV for Fe_2O_3 to 0.32 eV for Fe_2O_3-rGO (indirect). The increase in the bandgap is caused by the quantum size effect. While the decrease of the bandgap in the visible region can be related to the localized states produced in the forbidden region because of the defects formed from the rGO sheets. The random distribution of the defects on the GO sheets causes random distribution in sp^2 carbon islands and this may be the reason of the change in the optical band gap [37]. An increase or decrease in the band gap depend upon the size of the sp^2 carbon islands. The tune of the band gap to 1.55 eV is in good accordance with range of the Solar System.

Table 3. Extracted direct bandgap (E_{gd}) and the calculated optical parameters.

Sample	E_{gd} (eV)	n_M	n_R	n_{HV}	n_{KS}	n_A	$\Delta\chi$	Λ	n
Fe_2O_3	1.7	2.734	3.030	2.848	2.837	3.060	0.457	1.486	3.066
Fe_2O_3-rGO	1.55	2.798	3.123	2.924	2.923	3.090	0.417	1.495	3.158

The refractive index gives an indication on materials reflectivity to be useful tool in the industrial applications. This optical parameter can be investigated by the following empirical relations regarding to the value of the band gap.

The moss relation [39],

$$n_M^4 \times E_g = 95 \text{ eV} \tag{4}$$

The Ravindra relation [40],

$$n_R = 4.084 - 0.62E_g \tag{5}$$

The Herve and Vandamme relation [40, 41],

$$n_{HV} = \sqrt{1 + \left(\frac{13.6\ eV}{E_g + 3.4\ eV}\right)^2} \tag{6}$$

Kumar and Singh equation [40, 41],

$$n_{KS} = 3.3668 \times E_g^{-0.32234} \tag{7}$$

Anani *et al* suggested that [40, 41],

$$n_A = 3.4 - 0.2E_g \tag{8}$$

The direct optical band gaps in the visible region were used to calculate the refractive index for every model and the results were tabulated in table 3.

It is obvious that the refractive index calculated from the various models increased with depositing the Fe_2O_3 on rGO sheet. Therefore, depositing Fe_2O_3 on rGO promotes a denser nature and a lower bandgap, which observed in changing the refractive index value. In another word, after the insertion of the rGO sheet to the matrix the crystallite size decreases, the surface area increases, and the density also increases. This causes the reflectivity of the material increases. Hence the refractive index increases as well.

An essential parameter that is important for the electronic and optical applications in industry, is the optical basicity and its correlation with the optical electronegativity of the materials. The empirical relation between the optical basicity (Λ), optical electronegativity ($\Delta\chi$), optical band gap (E_g), and refractive index (n) derived by Duffy and Reddy are as following [41, 42],

$$\Delta\chi = 0.2688E_g \tag{9}$$

$$\Lambda = 1.59 - 0.2279\Delta\chi \tag{10}$$

$$n = -\ln(0.102\Delta\chi) \tag{11}$$

The calculated values of Λ, $\Delta\chi$, and n are presented in table 2. The Λ value slightly increases while $\Delta\chi$ slightly decreases for Fe_2O_3 and Fe_2O_3-rGO, respectively. Furthermore, it is obvious that there is a good match between the results obtained for the refractive index using Ravindra and Annani equations and the equation expressed by Duffy.

4. Conclusion

Fe_2O_3 nanoparticles were prepared via the co-precipitation method, then successfully loaded on the GO sheets through ultra-sonication method. This method is effective not only due to the successful loading and attachment of the Fe_2O_3 to the surface of GO sheets, but also due to the successful reduction of the GO into rGO and increasing the stability of the Fe_2O_3-rGO nanocomposite. The XRD analysis confirmed the phase structure of the Fe_2O_3 and Fe_2O_3-rGO. The XRD and TEM analysis confirmed the nanoscale of the prepared samples. The Fe_2O_3 growth was restricted by rGO sheets according to the morphological analysis. The loading process of the Fe_2O_3 on the rGO surface was confirmed by the TEM as well as the FT-IR. Furthermore, the reduction of the GO into rGO was confirmed by the Raman and FT-IR spectra. All these analyses revealed the impact of the reduced graphene oxide on the Fe_2O_3 structure and their optical parameters. The optical band gap in the UV region was found to increase from 3.62 eV for Fe_2O_3 to 4.06 eV for Fe_2O_3-rGO due to the quantum size effect. The optical bandgap was found to decrease from 1.7 eV for Fe_2O_3 to 1.55 eV for Fe_2O_3-rGO in the visible region. The tune of

the band gap to 1.55 eV is in good accordance with range of the Solar System. Also, the optical electronegativity was found to decrease while the optical basicity and refractive index were found to increase by the addition of rGO in Fe_2O_3 matrix. In conclusion the Fe_2O_3-rGO nanocomposite can be considered a perfect contender for a variety of applications, including solar cells.

Data availability statement

All data that support the findings of this study are included within the article (and any supplementary files).

ORCID iDs

T S Soliman https://orcid.org/0000-0001-7372-4761

References

[1] Shafiq M, Anjum S, Hano C, Anjum I and Abbasi B H 2020 An overview of the applications of nanomaterials and nanodevices in the food industry *Foods.* **9** 1–27
[2] Khan I, Saeed K and Khan I 2019 Nanoparticles: properties, applications and toxicities *Arab. J. Chem.* **12** 908–31
[3] Pandey S, Son N and Kang M 2022 Synergistic sorption performance of karaya gum crosslink poly(acrylamide-co-acrylonitrile) @ metal nanoparticle for organic pollutants *Int. J. Biol. Macromol.* **210** 300–14
[4] Jahan F, Uz Zaman S, Akhtar S, Arshad R, Ibrahim I M, Shahnaz G, Rahdar A and Pandey S 2021 Development of mucoadhesive thiomeric chitosan nanoparticles for the targeted ocular delivery of vancomycin against *Staphylococcus aureus* resistant strains *Nanofabrication.* **6** 16–24
[5] Kashyap K and Shekhawat G S 2022 Properties, particle-size, shape, synthesis, concentration and medium dependent toxicity of nanoparticles in plants *Toxicicity of Nanoparticles in Plants* (Academic Press, United Kingdom: Elsevier) 95–107
[6] Ivanov K V, Razorenov S V and Garkushin G V 2021 Investigation of structure and mechanical properties under quasi-static and planar impact loading of aluminum composite reinforced with Al_2O_3 nanoparticles of different shape *Mater. Today Commun.* **29** 102942
[7] Chandekar K V and Kant K M 2017 Effect of size and shape dependent anisotropy on superparamagnetic property of $CoFe_2O_4$ nanoparticles and nanoplatelets *Phys. B Condens. Matter.* **520** 152–63
[8] Mabrouk M, Das D B, Salem Z A and Beherei H H 2021 Nanomaterials for biomedical applications: production, characterisations, recent trends and difficulties *Molecules.* **26** 1–27
[9] Sargazi S, Siddiqui B, Qindeel M, Rahdar A, Bilal M, Behzadmehr R, Mirinejad S and Pandey S 2022 Chitosan nanocarriers for microRNA delivery and detection: a preliminary review with emphasis on cancer *Carbohydr. Polym.* **290** 119489
[10] Yadav H M, Kolekar T V, Pawar S H and Kim J S 2016 Enhanced photocatalytic inactivation of bacteria on Fe-containing TiO_2 *nanoparticles under fluorescent light, J. Mater. Sci. Mater. Med.* **27** 1–9
[11] Lorkit P, Panapoy M and Ksapabutr B 2014 Iron oxide-based supercapacitor from ferratrane precursor via sol–gel-hydrothermal process *Energy Procedia* **56** 466–73
[12] Chen W, Tao X, Li Y, Wang H, Wei D and Ban C 2016 Hydrothermal synthesis of graphene-MnO_2-polyaniline composite and its electrochemical performance *J. Mater. Sci., Mater. Electron.* **27** 6816–22
[13] Rahman M T, Asadul Hoque M, Rahman G T, Gafur M A, Khan R A and Hossain M K 2019 Study on the mechanical, electrical and optical properties of metal-oxide nanoparticles dispersed unsaturated polyester resin nanocomposites *Results Phys.* **13** 102264
[14] Rashad M 2020 Tuning optical properties of polyvinyl alcohol doped with different metal oxide nanoparticles *Opt. Mater. (Amst).* **105** 109857
[15] Xia C, Jia Y, Tao M and Zhang Q 2013 Tuning the band gap of hematite α-Fe_2O_3 by sulfur doping *Phys. Lett. Sect. A Gen. At. Solid State Phys.* **377** 1943–7
[16] Sephra P J, Baraneedharan P, Sivakumar M, Thangadurai T D and Nehru K 2018 *In situ* growth of hexagonal-shaped α-Fe_2O_3 nanostructures over few layered graphene by hydrothermal method and their electrochemical performance *J. Mater. Sci., Mater. Electron.* **29** 6898–908
[17] Biswal S, Bhaskaram D S and Govindaraj G 2020 α-Fe_2O_3/reduced graphene oxide nanocomposite: interfacial effect on the magnetic property *J. Supercond. Nov. Magn.* **33** 1629–32
[18] Yavuz C and Erten-Ela S 2022 Solar light-responsive α-Fe_2O_3/CdS/g-C_3N_4 ternary photocatalyst for photocatalytic hydrogen production and photodegradation of methylene blue *J. Alloys Compd.* **908** 164584
[19] Li P, Zhu B, Li P, Zhang Z, Li L and Gu Y 2019 A facile method to synthesize CdSe-reduced graphene oxide composite with good dispersion and high nonlinear optical properties *Nanomaterials.* **9** 957
[20] Sehrawat A P, Islam S S, Mishra P and Ahmad S 2018 Reduced graphene oxide (rGO) based wideband optical sensor and the role of Temperature, Defect States and Quantum Efficiency *Scientific Reports* **8** 3537
[21] Zhao M 2018 Direct synthesis of graphene quantum dots with different fluorescence properties by oxidation of graphene oxide using nitric acid *Appl. Sci.* **8** 1303
[22] Awad M M, Abdel-Salam A I, Elfeky S A, Rady H S, Hassanien A S, Mohamed M B and Elbashar Y H 2019 Tuning the optical properties of CdSe quantum dot using graphene nanocomposite *J. Opt.* **48** 616–25
[23] Abdel-Salam A I, Awad M M, Soliman T S and Khalid A 2022 The effect of graphene on structure and optical properties of CdSe nanoparticles for optoelectronic application *J. Alloys Compd.* **898** 162946
[24] Guo Q, Zheng Z, Gao H, Ma J and Qin X 2013 SnO_2/graphene composite as highly reversible anode materials for lithium ion batteries *J. Power Sources* **240** 149–54
[25] Nosheen E, Shah S M and Iqbal Z 2017 Ru-dye grafted CdS and reduced graphene oxide Ru/CdS/rGO composite: an efficient and photo tuneable electrode material for solid state dye sensitized polymer solar cells *J. Photochem. Photobiol. B Biol.* **167** 117–27
[26] Geerthana M, Prabhu S, Harish S, Navaneethan M, Ramesh R and Selvaraj M 2022 Design and preparation of ternary α-Fe_2O_3/SnO_2/rGO nanocomposite as an electrode material for supercapacitor *J. Mater. Sci., Mater. Electron.* **33** 8327–43

[27] Tobaldi D M, Sever Škapin A, Pullar R C, Seabra M P and Labrincha J A 2013 Titanium dioxide modified with transition metals and rare earth elements: phase composition, optical properties, and photocatalytic activity *Ceram. Int.* **39** 2619–29
[28] Farahmandjou M and Soflaee F 2015 Synthesis and characterization of α-Fe_2O_3 nanoparticles by simple co-precipitation method *Phys. Chem. Res.* **3** 191–6
[29] Marcano D C, Kosynkin D V, Berlin J M, Sinitskii A, Sun Z, Slesarev A, Alemany L B, Lu W and Tour J M 2010 Improved synthesis of graphene oxide *ACS Nano.* **4** 4806–14
[30] Nath D, Singh F and Das R 2020 X-ray diffraction analysis by williamson-hall, halder-wagner and size-strain plot methods of CdSe nanoparticles- a comparative study *Mater. Chem. Phys.* **239** 122021
[31] Mote V, Purushotham Y and Dole B 2012 Williamson-Hall analysis in estimation of lattice strain in nanometer-sized ZnO particles *J. Theor. Appl. Phys.* **6** 2–9
[32] Abdel-Aal S K, Ionov A, Mozhchil R N and Naqvi A H 2018 Simple synthesis of graphene nanocomposites MgO–rGO and Fe_2O_3–rGO for multifunctional applications *Appl. Phys. A Mater. Sci. Process.* **124** 1–10
[33] Li H, Zhao Q, Li X, Zhu Z, Tade M and Liu S 2013 Fabrication, characterization, and photocatalytic property of α-Fe_2O_3/graphene oxide composite *J. Nanoparticle Res.* **15** 1–11
[34] Kim S, Han K I, Lee I G, Park W K, Yoon Y, Yoo C S, Yang W S and Hwang W S 2016 A gallium oxide-graphene oxide hybrid composite for enhanced photocatalytic reaction *Nanomaterials.* **6** 3–7
[35] Sobhanardakani S, Jafari A, Zandipak R and Meidanchi A 2018 Removal of heavy metal (Hg(II) and Cr(VI)) ions from aqueous solutions using Fe_2O_3@SiO_2 thin films as a novel adsorbent *Process Saf. Environ. Prot.* **120** 348–57
[36] Han Y, Luo Z, Yuwen L, Tian J, Zhu X and Wang L 2013 Synthesis of silver nanoparticles on reduced graphene oxide under microwave irradiation with starch as an ideal reductant and stabilizer *Appl. Surf. Sci.* **266** 188–93
[37] de Lima A H *et al* 2020 Origin of optical bandgap fluctuations in graphene oxide *The European Physical Journal B* **93** 105
[38] Ali F M 2019 Structural and optical characterization of [(PVA:PVP)-Cu2+] composite films for promising semiconducting polymer devices *J. Mol. Struct.* **1189** 352–9
[39] Moss T S 1985 Relations between the refractive index and energy gap of Semiconductors *Phys. Status Solidi* **131** 415–27
[40] Ravindra N M, Ganapathy P and Choi J 2007 Energy gap-refractive index relations in semiconductors - An overview *Infrared Phys. Technol.* **50** 21–9
[41] Indolia R S 2017 Relationship of refractive index with optical energy gap and average energy gap for II-VI and III-V group of semiconductors *Int. J. Pure Appl. Phys.* **13** 185–91
[42] Duffy J A and Ingram M D 1992 Comments on the application of optical basicity to glass *J. Non. Cryst. Solids.* **144** 76–80